Environmental Science & Technology

Article

Cite This: Environ. Sci. Technol. 2018, 52, 12685−12696

pubs.acs.org/est

Oxygen Vacancies Induced by Transition Metal Doping in γ-MnO_2 for Highly Efficient Ozone Decomposition

Xiaotong Li,[†,∥] Jinzhu Ma,[*,†,‡,§] Li Yang,[†,⊥] Guangzhi He,[†,§] Changbin Zhang,[†,§] Runduo Zhang,[∥] and Hong He[†,‡,§]

[†]State Key Joint Laboratory of Environment Simulation and Pollution Control, Research Center for Eco-Environmental Sciences, Chinese Academy of Sciences, Beijing 100085, China

[‡]Center for Excellence in Regional Atmospheric Environment, Institute of Urban Environment, Chinese Academy of Sciences, Xiamen 361021, China

[§]University of Chinese Academy of Sciences, Beijing 100049, China

[∥]State Key Laboratory of Chemical Resource Engineering, Beijing University of Chemical Technology, Beijing 100029, China

[⊥]Engineering & Technology Research Center for Environmental Protection Materials and Equipment of Jiangxi Province, Pingxiang University, Pingxiang 337055, China

Supporting Information

ABSTRACT: Transition metal (cerium and cobalt) doped γ-MnO_2 (M-γ-MnO_2, where M represents Ce, Co) catalysts were successfully synthesized and characterized. Cerium-doped γ-MnO_2 materials showed ozone (O_3) conversion of 96% for 40 ppm of O_3 under relative humidity (RH) of 65% and space velocity of 840 L g^{-1} h^{-1} after 6 h at room temperature, which is far superior to the performance of the Co-γ-MnO_2 (55%) and γ-MnO_2 (38%) catalysts. Under space velocity of 840 L g^{-1} h^{-1}, the conversion of ozone over the Ce-γ-MnO_2 catalyst under RH = 65% and dry conditions within 96 h was 60% and 100%, respectively, indicating that it is a promising material for ozone decomposition. XRD and HRTEM data suggested that Ce-γ-MnO_2 formed mixed crystals consisting of α-MnO_2 and γ-MnO_2 with specific surface area increased from 74 m^2/g to 120 m^2/g compared to undoped γ-MnO_2, thus more surface defects were introduced. H_2-TPR, O_2-TPD, XPS, Raman, and EXAFS confirmed that Ce-γ-MnO_2 exhibited more surface oxygen vacancies and surface defects, which play a key role during the decomposition of ozone. This study provides important insights for developing improved catalysts for gaseous ozone decomposition and promoting the performance of manganese oxide for practical ozone elimination.

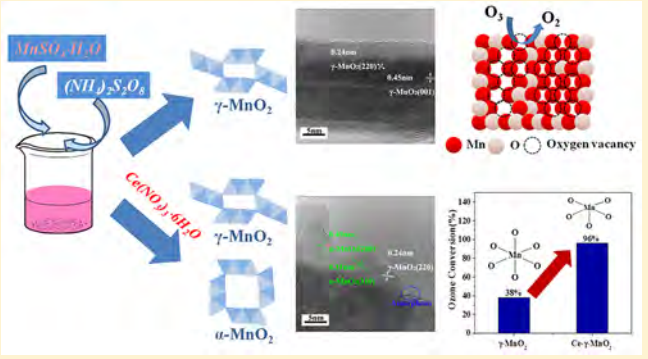

1. INTRODUCTION

In recent years, ozone pollution in the atmosphere has become more and more serious in both developing and developed countries.[1,2] The photochemical reactions involving volatile organic compounds (VOCs) and nitrogen oxides (NOx) driven by sunlight will increase the outdoor O_3 concentration,[3] and the generated ozone induces the aging of building materials, decreases crop yield, and causes the deceleration of tree growth.[1,2] The sources of indoor ozone mainly consist of ozone-generating air cleaning devices (OACD)[4] and modern office equipment involving high-pressure discharge, corona discharge, or ultraviolet radiation (such as photocopiers and laser-jet printers).[5] Long-term exposure to ozone will bring about many kinds of detrimental effects including neurological diseases,[6] decreased pulmonary function and airway inflammation,[7] high blood pressure,[8] and accelerated aging.[9] Besides, indoor ozone can produce a series of oxidation products including unsaturated hydrocarbons, VOCs, and secondary organic aerosol (SOA), which are more harmful to humans than ozone itself.[4] Thus, the U.S. Environmental Protection Agency (EPA) updated the National Ambient Air Quality Standards (NAAQS) limit for ground-level ozone from 75 to 70 ppb. Therefore, the study of ozone decomposition is of great significance for environmental conservation and human health.

A variety of techniques have been applied in ozone treatment, such as thermal decomposition, adsorption, electromagnetic wave radiation, and catalytic decomposition. Among them, catalytic decomposition has advantages in terms of safety, economy, and efficiency, so it is widely used to remove ozone. The catalysts used mainly consist of noble metals (e.g.,

Received: August 2, 2018
Revised: September 28, 2018
Accepted: October 12, 2018
Published: October 12, 2018

DOI: 10.1021/acs.est.8b04294
Environ. Sci. Technol. 2018, 52, 12685−12696

Ag,[10,11] Au,[12,13] and Pd[14,15]) and transition metal oxides (e.g., MnO_2,[16] Co_3O_4,[17] Cu_2O,[18,19] Fe_2O_3,[20,21] and NiO[22]). Among these catalysts, manganese oxide is a highly efficient and economical catalyst for catalytic decomposition of ozone.[23,24] Manganese dioxides show great structural flexibility and a number of crystallographic polymorphs such as α-, β-, γ-, and δ-MnO_2, which all contain edge- or corner-sharing [MnO_6] octahedra.[25] Among all the research works, α-MnO_2 has been most commonly studied due to its excellent activity for ozone decomposition.[16,26] α-MnO_2 possesses a one-dimensional tunnel structure composed of 2 × 2 edge-shared MnO_6 octahedral chains, which are corner-connected to form 4.6 × 4.6 Å tunnels.[27] γ-MnO_2 is also a form of manganese dioxide with a one-dimensional tunnel structure consisting of disordered 1 × 1 and 1 × 2 tunnels made up of edge-shared MnO_6 octahedral chains, which are corner-connected to form 1.89 × 1.89 Å and 2.3 × 4.6 Å tunnels.[28] Furthermore, γ-MnO_2 has been applied in the catalytic decomposition of formaldehyde, toluene, and NO_x because of its excellent performance, low-cost raw material, and low toxicity.[29−32] However, the catalytic decomposition of gaseous O_3 over γ-MnO_2 has rarely been reported. Jia et al.[28] reported that the ozone conversion over γ-MnO_2 can reach 95% under dry conditions at room temperature, but its performance under humid conditions was not studied. Nevertheless, the ozone decomposition performance of manganese oxides is greatly restricted by humidity.[33]

Jia et al.[28] also found that the content of oxygen vacancies determined the activity of manganese dioxides with different crystal structures (α-, β-, and γ-MnO_2), and oxygen vacancies are considered to be active sites for ozone decomposition. According to previous reports, doping with specific transition metals during hydrothermal synthesis will disturb the normal formation of MnO_2 and facilitate the formation of oxygen vacancies.[34,35] Ma et al.[36] found that doping with Ce^{3+} during the hydrothermal synthesis of OMS-2 materials will replace the ions in the tunnel and framework of the cryptomelane structure, which will give rise to an increase in Mn^{3+} (along with oxygen vacancies) and surface defects. Liu et al.[37] found that the addition of Ce^{3+} during the hydrothermal synthesis of todorokite MnO_2 changes the morphology from agglomerated particles to small sheets, resulting in larger surface area, and leads to the appearance of crystal boundaries between MnO_2 and CeO_2, which gives rise to the formation of more oxygen vacancies. Jia et al.[38] indicated that doping with Fe^{3+} during the hydrothermal synthesis of MnO_2 led to the original product α-MnO_2, with [2 × 2] tunnels, totally transforming into ramsdellite MnO_2 with [1 × 2] tunnels, and generated some Fe_2O_3 at the same time; this led to an increase in the specific surface area and more oxygen vacancies. In this study, the addition of Ce^{3+} during the hydrothermal synthesis of γ-MnO_2 induced some γ-MnO_2 to convert into α-MnO_2, resulting in the formation of mixed crystals, which increased the specific surface area and the content of oxygen vacancies. Therefore, the Ce-modified γ-MnO_2 catalyst has better performance and practical potential than unmodified γ-MnO_2.

2. EXPERIMENTAL SECTION

Preparation of Catalysts. The γ-MnO_2 materials were synthesized by reaction between $MnSO_4{\cdot}H_2O$ and $(NH_4)_2S_2O_8$ via a one-step hydrothermal method according to a previous report.[39] The detailed preparation procedure of γ-MnO_2 catalysts is as follows: 3.375 g of $MnSO_4{\cdot}H_2O$ was dissolved in 80 mL of deionized water under stirring, then 4.575 g of $(NH_4)_2S_2O_8$ was added, followed by stirring magnetically for about 30 min until the solution became homogeneous, after which it was transferred into a 100 mL Teflon-lined stainless-steel autoclave. The autoclave was kept at 90 °C for 24 h in an oven and then cooled to room temperature. After discarding the supernatant, the resulting products were obtained by filtering, washing, drying at 80 °C for 12 h, and calcining at 300 °C for 2 h. The synthetic procedures for Co-γ-MnO_2 and Ce-γ-MnO_2 were similar to that for γ-MnO_2 with the exception of adding $Co(NO_3)_3{\cdot}6H_2O$ or $Ce(NO_3)_3{\cdot}6H_2O$ to the initial solution. In order to determine the optimal doping ratio, we prepared catalysts with different initial Ce/Mn weight ratios (0, 1/10, 1/8, and 1/6). The sample with Ce/Mn = 1/8 had the highest ozone conversion (Figure S1). Therefore, catalysts with M/Mn = 1/8 (where M represents Ce, Co) and named M-γ-MnO_2 were the main materials synthesized. The α-MnO_2 materials were synthesized by reaction between $MnSO_4{\cdot}H_2O$ and $KMnO_4$ via a one-step hydrothermal method according to a previous report.[39] The subsequent procedures were similar to that followed for γ-MnO_2. The α+γ-MnO_2 catalyst was obtained by mixing equal weights of α-MnO_2 and γ-MnO_2 catalysts.

Catalyst Characterization. The crystalline structure was measured by a Bruker D8-Advance X-ray powder diffractometer using Cu Kα (λ = 0.15406 nm) radiation at a tube voltage of 40 kV and current of 40 mA in the 2θ range 10°−80° with a step size of 0.02°. The specific surface areas and pore structures of the catalysts were obtained using a Quantachrome physisorption analyzer at 77K. The morphologies of the γ-MnO_2 and M-γ-MnO_2 catalysts were observed with a SU8020 field emission scanning electron microscope (FESEM) using the accelerating voltage of 3 kV. The elemental distribution was measured by an EDX detector in the FESEM. The lattice images were taken using high-resolution TEM (TEM-2100 Plus Electron Microscope) at an accelerating voltage of 200 kV. Temperature-programmed H_2 reduction (H_2-TPR) experiments were conducted using an AutoChemII 2920 Chemisorption Analyzer (Micromeritics) equipped with a TCD detector. The desorption of oxygen was obtained by a temperature-programmed desorption of O_2 experiment, and the signal for O_2 was detected with a mass spectrometer. The contents of different oxygen species were determined using an Imaging X-ray Photoelectron Spectrometer (Axis Ultra, Kratos Analytical Ltd.). Raman spectra of the γ-MnO_2 and M-γ-MnO_2 catalysts were recorded on a homemade UV resonance Raman spectrometer (UVRDLPC-DL-03) and a CCD detector cooled by liquid nitrogen. The surface defects were determined by measuring the X-ray absorption near edge structure (XANES) and extended X-ray absorption fine structure (EXAFS) of the Mn−K edge in the γ-MnO_2 catalysts.

Catalytic Activity. The activity of the γ-MnO_2 and M-γ-MnO_2 catalysts for ozone decomposition was measured in a fixed-bed continuous flow quartz reactor (4 mm i.d.) using about 100 mg of catalyst with size of 40−60 mesh at room temperature (30 °C). The gas flow passing through the reactor was 1400 mL/min, and the weight space velocity was calculated to be 840 $L{\cdot}g^{-1}{\cdot}h^{-1}$. The relative humidity of the gas stream was maintained at 65% by controlling the flow of wet gas and measured with a humidity probe (HMP110, Vaisala OYJ). The ozone was generated by low-pressure ultraviolet lamps, and the concentration was maintained at 40

DOI: 10.1021/acs.est.8b04294
Environ. Sci. Technol. 2018, 52, 12685−12696

± 2 ppm. An ozone monitor (Model 202, 2B Technologies) was used to monitor the inlet and outlet ozone concentrations. The ozone conversion was calculated by the following equation

$$O_3 \text{ conversion} = \frac{C_{in} - C_{out}}{C_{in}} \times 100\%$$

where C_{in} and C_{out} are inlet and outlet concentrations of ozone, respectively.

3. RESULTS AND DISCUSSION

3.1. The Crystal Structures and Surface Areas of the Catalysts. The XRD patterns of the as-prepared catalysts are shown in Figure 1. The pattern of pure γ-MnO_2 corresponds

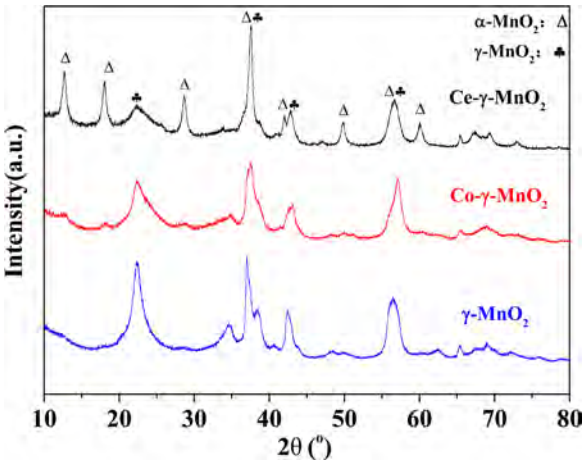

Figure 1. XRD patterns of the γ-MnO_2 and M-γ-MnO_2 catalysts.

well to the standard PDF card (JCPDS 14-0644) of γ-MnO_2. The diffraction peaks of CeO_2 or Co_3O_4 were not observed for the M-γ-MnO_2 catalysts, which revealed that the content of CeO_2 or Co_3O_4 was below the detection limits of the XRD instrument, or was finely dispersed over the surface of the MnO_2. It was noted that the crystal structure of the Ce-γ-MnO_2 catalyst had changed. First, the corresponding diffraction peaks for γ-MnO_2 broadened and lessened in intensity, which indicated that doping with Ce is detrimental to the formation of γ-MnO_2.[40] In addition, the characteristic diffraction peaks for α-MnO_2 (JCPDS 44-0141) appeared, which showed that doping with Ce is favorable for the formation of α-MnO_2. Part of the γ-MnO_2 had transformed into α-MnO_2, forming a mixed crystal; thus, more surface defects were introduced.[37,41] The surface oxygen species are usually adsorbed on the defect sites, so a high defect density is conducive to the adsorption of ozone molecules on the surface of the catalyst.[33] The crystal structure of Co-γ-MnO_2 showed slight formation of α-MnO_2, and the most significant phenomenon was that the diffraction peaks were broadened and weakened in intensity compared to those of the γ-MnO_2 catalyst. Thus, the degree of crystallinity declined. The Co-γ-MnO_2 catalyst with poor crystallinity can generate more defects in the γ-MnO_2 framework structure, which is favorable to the adsorption and decomposition of ozone molecules. Therefore, it is reasonable that M-γ-MnO_2 might exhibit higher conversion of ozone compared with γ-MnO_2.

Figure S2 shows the N_2 adsorption−desorption isotherms of the γ-MnO_2 and M-γ-MnO_2 catalysts. The catalysts have similar N_2 adsorption/desorption isotherms, showing the characteristics of mesoporous materials. According to the IUPAC classification, the isotherms of the three catalysts belong to the type IV isotherm pattern, with the type H3 hysteresis loop, which is usually related to the accumulation of layered particles and the formation of slit-like pores.[42] The specific surface areas, pore size distributions, and pore volumes are shown in Table 1. Compared with the γ-MnO_2 and Co-γ-MnO_2 catalysts, Ce-γ-MnO_2 with an average pore diameter of 6.53 nm has a relatively small pore size distribution. The specific surface areas of the γ-MnO_2, Co-γ-MnO_2, and Ce-γ-MnO_2 catalysts were 74, 87, and 120 m^2/g, respectively. The specific surface area of Ce-γ-MnO_2 was markedly higher than those of Co-γ-MnO_2 and γ-MnO_2. A large specific surface area can expose more surface active sites, which is favorable for the adsorption of ozone molecules.

Table 1. BET Surface Area, Pore Structure, and FESEM Results of γ-MnO_2 and M-γ-MnO_2

	BET			FESEM	
catalysts	S_{BET} (m^2/g)	D_{pore} (nm)	V_{pore} (cm^3/g)	urchin sphere	compact sphere
γ-MnO_2	74	9.57	0.19	100%	0
Co-γ-MnO_2	87	9.57	0.21	40%	60%
Ce-γ-MnO_2	120	6.53	0.30	20%	80%

3.2. The Morphology and Elemental Distribution of the Catalysts. The morphologies and microstructures of the catalysts were observed by FESEM. The size distribution histograms of γ-MnO_2 and M-γ-MnO_2 are shown in Figure S3. As shown in Figure 2A and B, the γ-MnO_2 nanorods were assembled in a radially symmetric urchin-like structure 6.1 ± 1.2 μm in diameter.[39] Doping with transition metals had a big impact on the shape of γ-MnO_2, so that the urchin-like nanostructure partially transformed into compact globules, and the size of the globules changed at the same time. After doping with Co (Figure 2C, D, E, and F), the urchin-like nanostructures became larger, with a diameter of 7.4 ± 1.0 um, and the stretched nanorods became disorganized. In addition, there were about 60% compact globules with a diameter of 5.8 ± 1.4 μm. After doping with Ce (Figure 2G, H, I, and J), the urchin-like nanostructures became larger, with a diameter of 6.6 ± 1.2 um, and the stretched nanorods became thinner and longer. In addition, there were about 80% compact globules with a diameter of 5.3 ± 1.3 μm. During the in situ doping metal process, different metal ions will affect the normal synthesis of γ-MnO_2 and make the resultant materials different.

Elemental mapping was conducted to observe the element distribution of the doped metal within the M-γ-MnO_2 catalysts. The Ce mappings in Figure 3 show that the surface Ce atoms were dispersed as homogeneously as Mn within the urchin-like globules and the compact globules. However, the surface Co atoms were not dispersed as homogeneously as Mn within the urchin-like globules or the compact globules. As is shown in Table S1, the ICP results show that the content of Ce and Co is 2.97% and 0.4%, and the EDS results show the content of Ce and Co on the catalyst surface to be 8.07% and 10.38%, which indicates that the Ce or Co atoms are mainly concentrated on the surface of the catalysts.

DOI: 10.1021/acs.est.8b04294
Environ. Sci. Technol. 2018, 52, 12685−12696

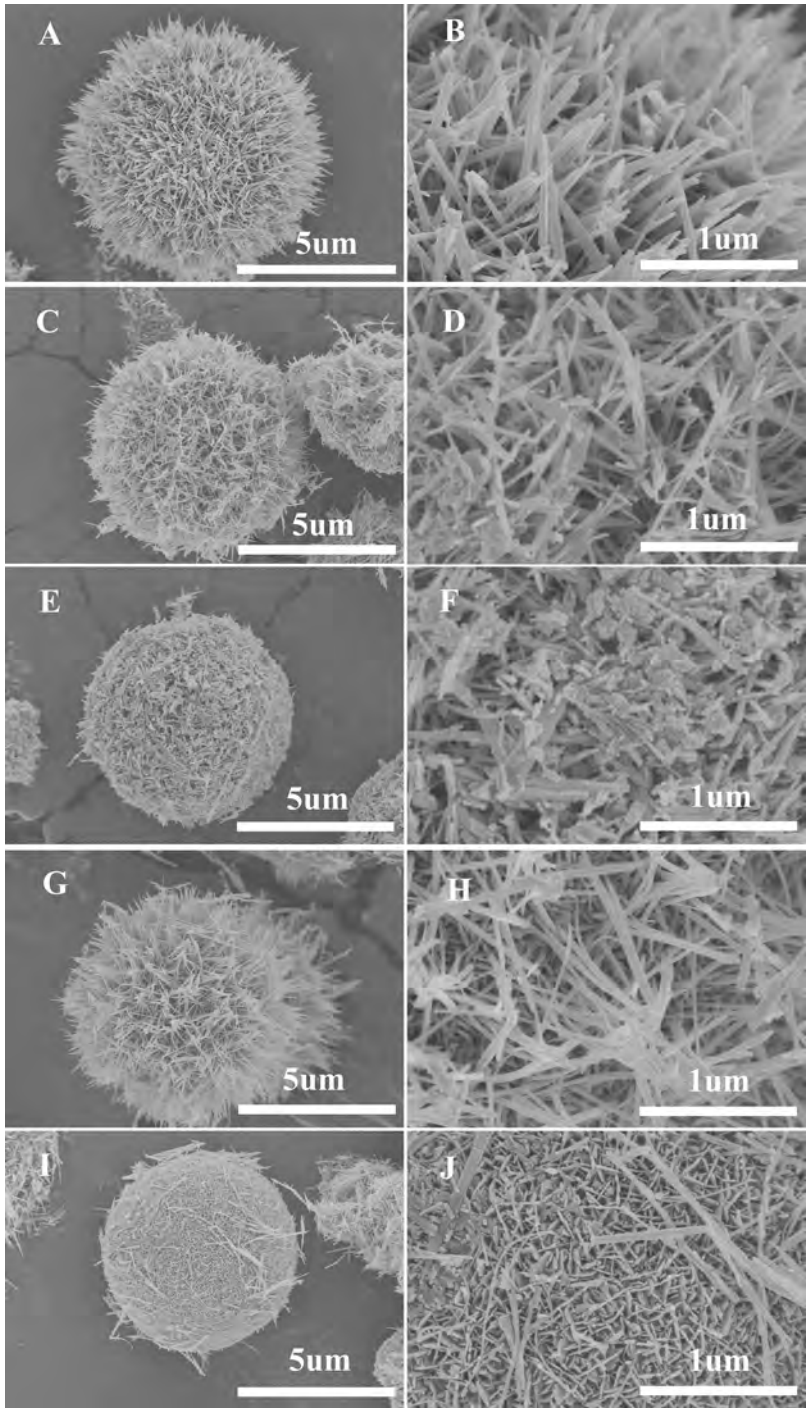

Figure 2. SEM images of catalysts: (A–B) γ-MnO_2, (C–F) Co-γ-MnO_2, and (G–J) Ce-γ-MnO_2.

The morphologies and microstructures of the catalysts were further investigated using HRTEM. As shown in Figure 4A, γ-MnO_2 displays fringe spacings of 0.24 and 0.45 nm representing the (220) and (001) planes of γ-MnO_2 and contains scarcely any amorphous regions. For M-γ-MnO_2 (Figure 4B and C), besides γ-MnO_2, the (200) and (310) planes of α-MnO_2 are also exhibited, as shown by fringe spacings of 0.49 and 0.31 nm, respectively. Furthermore, amorphous regions and obvious local lattice distortions visually appear in the HRTEM images, which can generate more surface defects.[43,44] The reason for the above phenomenon could be that doping with Ce or Co destroyed the normal growth of the crystals.[45] These results are consistent with the XRD results, which can further demonstrate the formation of mixed crystals and surface defects.

3.3. Reducibility of Catalysts. The H_2-TPR profiles (Figure 5) of the γ-MnO_2 and M-γ-MnO_2 catalysts were measured to evaluate their reducibility. The γ-MnO_2 and M-γ-MnO_2 catalysts all exhibit two principal reduction peaks (peak I and II). As shown in Table 2, the H_2 consumption of peak I is about twice that of peak II, so the samples could mainly follow a reduction route such that MnO_2 first transforms into Mn_3O_4, then to MnO.[46] The reduction peaks of γ-MnO_2 appeared at 272 and 385 °C. The low temperature reduction peak of Ce-γ-

DOI: 10.1021/acs.est.8b04294
Environ. Sci. Technol. 2018, 52, 12685–12696

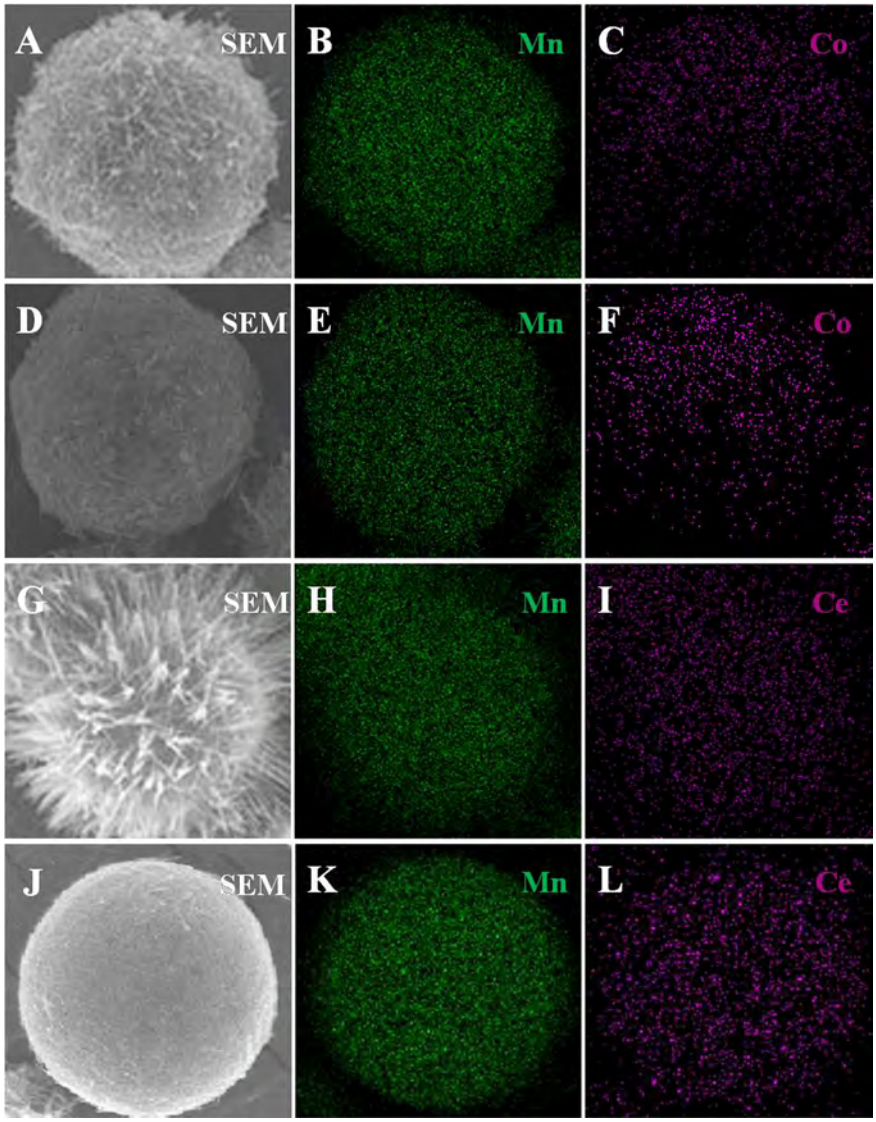

Figure 3. Elemental mapping of catalysts: (A–F) Co-γ-MnO_2 and (G–L) Ce-γ-MnO_2.

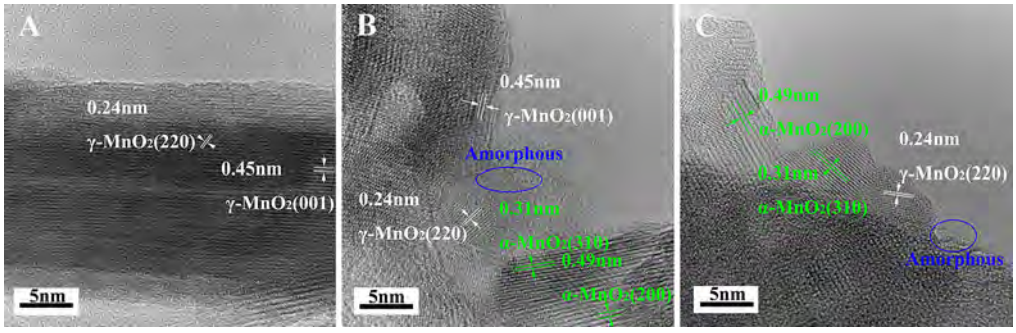

Figure 4. HRTEM images of catalysts: (A) γ-MnO_2, (B) Co-γ-MnO_2, and (C) Ce-γ-MnO_2.

MnO_2 could be observed at 265 °C, and the high temperature reduction peak occurred at 380 °C. The two reduction peaks of Co-γ-MnO_2 were at 263 and 377 °C, respectively, which was similar to the results for Ce-γ-MnO_2. For manganese oxide, the catalytic decomposition mechanism of ozone mainly includes the adsorption of ozone on the catalyst surface, the redox process, and the desorption of the decomposition products. The position of the first reduction peak can indicate the reducibility of the catalysts. The first reduction peak of the Ce-γ-MnO_2 and Co-γ-MnO_2 catalysts appears at lower temperature, which show they have higher reducibility; thus, their activity should be superior to that of γ-MnO_2. Table 2 shows the total amounts of consumed H_2. The H_2 consumption of both the Ce-γ-MnO_2 and Co-γ-MnO_2 catalysts was lower than that of γ-MnO_2, which illustrates that a certain amount of Mn^{3+} is present in the catalysts and that the Mn^{3+} content of Ce-γ-

DOI: 10.1021/acs.est.8b04294
Environ. Sci. Technol. 2018, 52, 12685–12696

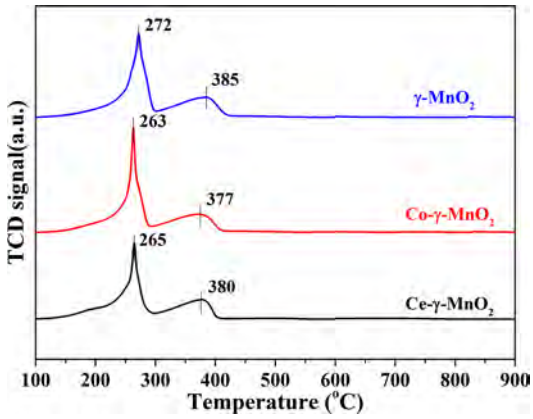

Figure 5. H_2-TPR profiles of the γ-MnO_2 and M-γ-MnO_2 catalysts.

Table 2. H_2-TPR and O_2-TPD Results of γ-MnO_2 and M-γ-MnO_2

	H_2-TPR				O_2-TPD
catalysts	peak I (mmol/g)	peak II (mmol/g)	peak I/ peak II	total (mmol/g)	T < 350 °C (%)
γ-MnO_2	6.76	3.50	1.93	10.26	0
Co-γ-MnO_2	6.19	3.21	1.93	9.40	13.53
Ce-γ-MnO_2	5.76	2.98	1.93	8.74	14.12

MnO_2 is higher than of Co-γ-MnO_2. It is generally known that oxygen vacancies will be created to maintain charge balance when Mn^{3+} exists in manganese dioxide on the basis of the following process (R1)[28]

$$4Mn^{4+} + O^{2-} \rightarrow 4Mn^{4+} + 2e^-/V_O + \frac{1}{2}O_2 \rightarrow 2Mn^{4+} + 2Mn^{3+} + V_O + \frac{1}{2}O_2 \quad \text{(R1)}$$

where V_O represents an oxygen vacancy site. Therefore, it can be deduced that the surface oxygen vacancy density increases in the order γ-MnO_2 < Co-γ-MnO_2 < Ce-γ-MnO_2.

3.4. The Characteristics of Oxygen Vacancies. The evolution of oxygen was characterized by an O_2-TPD experiment, and the results are shown in Figure 6A. The desorption capacity of the oxygen species on the surface of the catalyst was observed by detecting the O_2 desorption peak using mass spectrometry. The chemisorbed oxygen species and active surface oxygen usually desorb at lower temperatures around 350 °C, and the higher temperature desorption peak (500−650 °C) is ascribed to the subsurface lattice oxygen.[26] The higher temperature peak at 700 °C is attributed to the conversion of bulk lattice oxygen.[26] The lower the temperature at which oxygen is released, the looser it is bound to Mn atoms within the framework. Therefore, the Ce-γ-MnO_2 and Co-γ-MnO_2 catalysts had higher oxygen mobility.[45] As shown in Figure 6A, the total peak areas for Ce-γ-MnO_2 are visibly larger than for the γ-MnO_2 and Co-γ-MnO_2 catalysts, indicating that the former had more excellent oxygen adsorption and storage capacity. As shown in Table 2, abundant active oxygen species exist in the Ce-γ-MnO_2 and Co-γ-MnO_2 catalysts, and the content of active oxygen species on the Ce-γ-MnO_2 catalyst is higher than that of Co-γ-MnO_2. However, there are almost no surface oxygen species in γ-MnO_2. The result indicates that the Ce-γ-MnO_2 catalyst has more surface-adsorbed oxygen (O^{2-}, O^-, OH^-), which is consistent with the results of H_2-TPR since oxygen species are typically adsorbed on the oxygen vacancies.[47] The adsorption and desorption of oxygen over the catalysts were tested, and the results are shown in Figure S4. When the temperature was increased from room temperature to 450 °C, an oxygen desorption peak at 450 °C was observed. When the catalysts began to cool from 450 °C, an oxygen adsorption peak was observed. The cycles of heating and cooling were repeated four times, and the oxygen adsorption and desorption of Ce-γ-MnO_2 during every cycle were greater than that of γ-MnO_2 and Ce-γ-MnO_2, which indicates that the capacity for oxygen adsorption and desorption of Ce-γ-MnO_2 is greater.

Figure 6B shows the XPS spectra in the O 1s region. The O 1s spectra can be deconvoluted into three peaks to gain information on the nature of oxygen species. The peak at ∼529.7 eV can be ascribed to the lattice oxygen (denoted as O_I), the peak at binding energy of ∼531.2 eV is assigned to the surface-adsorbed oxygen species (denoted as O_{II}), and the peak at the higher binding energy of ∼533.5 eV can be assigned to the surface-adsorbed water (denoted as O_{III}).[48] Table 2 shows that the content of the surface-adsorbed oxygen species (O_{II}) decreases in the sequence Ce-γ-MnO_2 (32.57%) > Co-γ-MnO_2 (30.65%) > γ-MnO_2 (30.10%). This result further confirmed that the Ce-γ-MnO_2 catalyst has more surface oxygen vacancies, which is consistent with the results revealed by H_2-TPR and O_2-TPD.

The XPS spectra of Mn $2p_{3/2}$ are shown in Figure 6C. Deconvolution of the Mn $2p_{3/2}$ peaks indicates that there are two manganese species in the three catalysts. The two peaks at 641.8 and 642.7 eV are attributed to Mn^{3+} and Mn^{4+}, respectively.[16,28] The Mn^{3+}/Mn^{4+} molar ratios are summarized in Table 3. The Ce-γ-MnO_2 catalyst has the highest Mn^{3+}/Mn^{4+} molar ratio (0.18), and the Mn^{3+}/Mn^{4+} molar ratios for the γ-MnO_2 and Co-γ-MnO_2 catalysts are 0.11 and 0.12, respectively. Therefore, the Ce-γ-MnO_2 catalyst has more oxygen vacancies. As shown in Figure 6D, the average oxidation state (AOS) of Mn was calculated by the following formula: AOS = 8.956 − 1.126ΔE_s, where ΔE_s represents the binding energy difference between the two Mn 3s peaks.[28] The AOS of the Ce-γ-MnO_2 catalyst is the lowest (3.62), which suggests that the content of Mn^{3+} in Ce-γ-MnO_2 is the highest. The above results further demonstrate that Ce-γ-MnO_2 has more oxygen vacancies than the other catalysts.

Compared with XPS, Raman spectroscopy mainly shows the bulk structure of catalysts. Figure 7 shows the Raman spectra of the γ-MnO_2 and M-γ-MnO_2 catalysts. The γ-MnO_2 catalysts showed bands at 197, 260, 370, 524, 572, and 652 cm^{-1}, which is consistent with the previous data on γ-MnO_2.[49] The first three bands are attributed to the deformation vibration of the metal−oxygen chain of Mn−O−Mn, and the latter three correspond to the stretching vibration of the MnO_6 octahedron.[16,50] Among all the bands, the peak at 572 cm^{-1} is indicative of a well-developed orthorhombic structure with an interstitial space consisting of (1 × 2) channels.[28,51] The first band at 197 cm^{-1} shifts to 204 and 218 cm^{-1} for Co-γ-MnO_2 and Ce-γ-MnO_2, respectively. Meanwhile the last band at 652 cm^{-1} shifts to 644 cm^{-1} for Ce-γ-MnO_2. The above peak-shift phenomenon indicated the formation of α-MnO_2.[28,49] The results are consistent with the XRD patterns and HRTEM images. Compared with γ-MnO_2, the bands of Ce-γ-MnO_2 catalysts became broader and weaker. The above

DOI: 10.1021/acs.est.8b04294
Environ. Sci. Technol. 2018, 52, 12685−12696

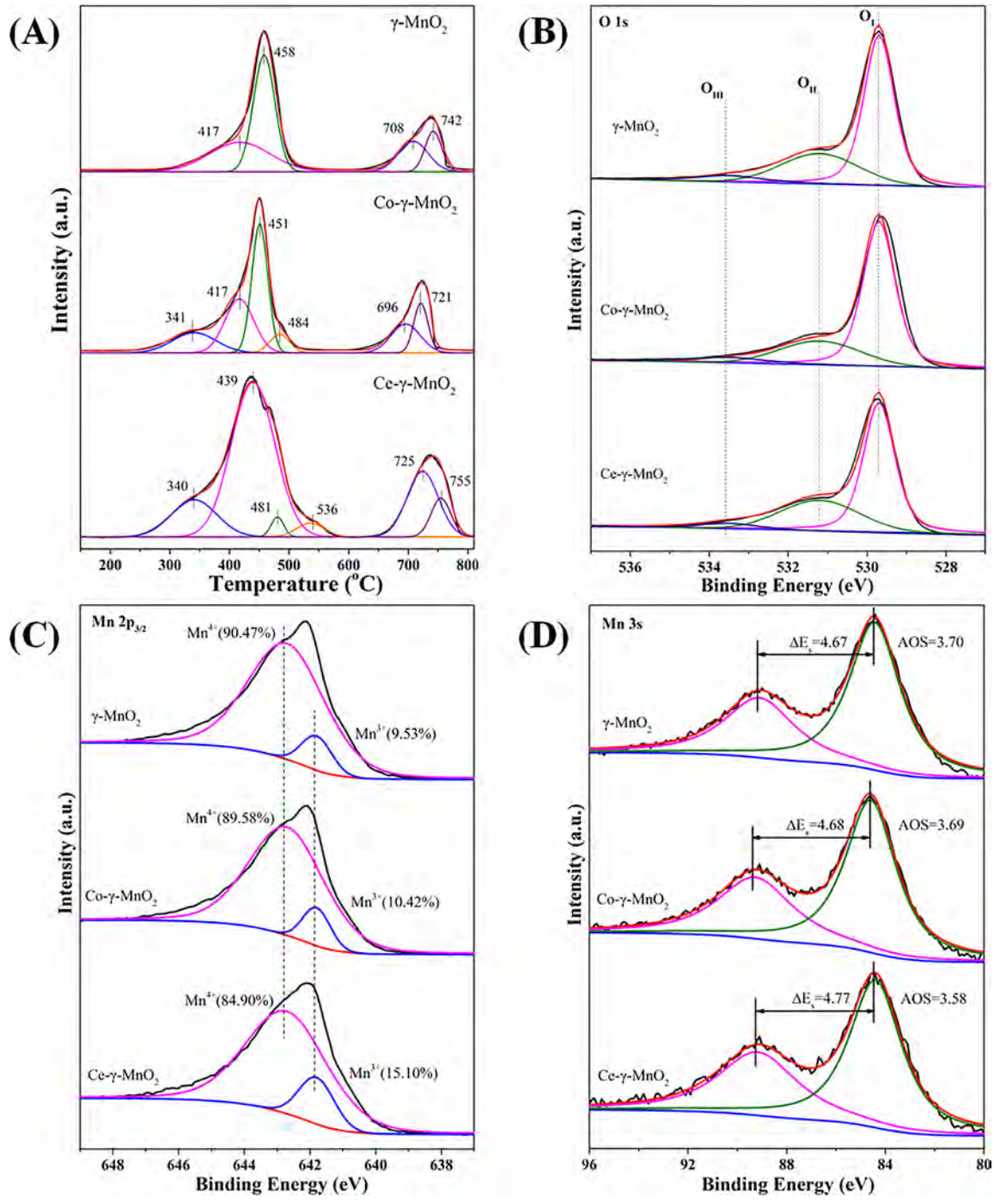

Figure 6. (A) O_2-TPD profiles of the γ-MnO_2 and M-γ-MnO_2 catalysts and (B) O 1s, (C) Mn 2p, and (D) Mn 3s XPS spectra of the γ-MnO_2 and M-γ-MnO_2.

Table 3. XPS Results of γ-MnO_2 and M-γ-MnO_2

	O 1s			Mn $2p_{3/2}$			Mn 3s
catalysts	O_I (%)	O_{II} (%)	O_{III} (%)	Mn^{3+} (%)	Mn^{4+} (%)	Mn^{3+}/Mn^{4+}	AOS of Mn
γ-MnO_2	60.75	30.10	9.15	9.53	90.47	0.11	3.70
Co-γ-MnO_2	58.97	30.65	10.38	10.42	89.58	0.12	3.69
Ce-γ-MnO_2	57.61	32.57	9.81	15.10	84.90	0.18	3.62

results showed that Ce-doping increased the disorder of the interior lattice structure and led to the regular γ-MnO_2 crystals transforming into an amorphous structure, which could lead to the formation of oxygen vacancies.[52−54] Therefore, the Ce-γ-MnO_2 catalysts had the most oxygen vacancies, which is consistent with the H_2-TPR and O_2-TPD results.

X-ray absorption fine structure spectroscopy (XAFS) can be used to explore the surface defects, local atomic arrangement, and electronic structure of crystalline materials. Therefore, X-ray absorption fine structure spectroscopy (XAFS) measurements were carried out to further examine the distinct oxygen vacancy concentrations in the γ-MnO_2 and M-γ-MnO_2 catalysts. The Mn *K*-edge $k^3\chi(k)$ oscillation curves (Figure 8A) of Co-γ-MnO_2 and Ce-γ-MnO_2 were similar to that of γ-

DOI: 10.1021/acs.est.8b04294
Environ. Sci. Technol. 2018, 52, 12685−12696

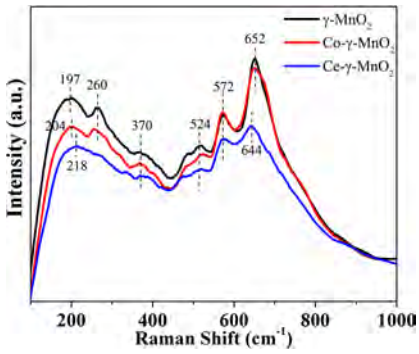

Figure 7. Raman spectra of the γ-MnO_2 and M-γ-MnO_2 catalysts.

MnO_2, which indicated that the [MnO_6] octahedral structure is well maintained.[45] The corresponding Fourier-transformed $k^3\chi(k)$ functions (Figure 8B) can reveal differences in the coordination environment of the Mn atoms. The FT curves have three main peaks at 1.89, 2.89, and 3.4 Å, corresponding to the Mn−O, Mn−Mn_1, and Mn−Mn_2 coordination shells, respectively.[33,36] The peak intensity for Mn−O coordination in Ce-γ-MnO_2 clearly decreased in comparison with γ-MnO_2 and Co-γ-MnO_2, qualitatively illustrating its lowered Mn−O coordination (increased oxygen vacancies).[45,55,56] Meanwhile, the peak intensity for Mn−Mn_1 and Mn−Mn_2 coordination in Ce-γ-MnO_2 and Co-γ-MnO_2 showed a distinct decrease, and that in Ce-γ-MnO_2 decreased more markedly.

Least-squares curve fitting was conducted to obtain quantitative structural parameters around Mn atoms in the γ-MnO_2 and M-γ-MnO_2 single-unit-cell layers. Ramsdellite γ-MnO_2 with orthorhombic structure (space group *Pnam*) was used as the reference model, and its single and multiple scattering paths were used to fit the EXAFS data. The crystal structure of the reference material is listed in Table S2. The EXAFS data fitting results are shown in Figure S5 and Table 4. The reference material (γ-MnO_2) was confirmed to possess perfect coordination, such that the Mn−O, Mn−Mn_1, and Mn−Mn_2 coordination shells at *ca.* 1.89, 2.89, and 3.4 Å have coordination numbers of 6.0, 4.0, and 4.0, respectively. The coordination numbers for Mn−O, Mn−Mn_1, and Mn−Mn_2 coordination, confined in the Ce-γ-MnO_2 and Co-γ-MnO_2 single-unit-cell layers, decreased as compared with the γ-MnO_2 single-unit-cell layers, which indicates that these catalysts possessed more surface defects.[33,36] Among them, the Mn−O coordination number of Ce-γ-MnO_2 and Co-γ-MnO_2 decreased to 5.3 and 5.7, respectively, which further indicated that more oxygen vacancies had formed in their structure. This will facilitate the adsorption and activation of ozone. The

Table 4. Curve-Fitting Results of Mn K-Edge EXAFS in γ-MnO_2 and M-γ-MnO_2 Catalysts

catalysts	Mn−K reference	shell	CN[a]	R[b] (Å)	DW[c] (10^{-3} Å^2)	R factor (%)
γ-MnO_2	γ-MnO_2	Mn−O	6	1.89	3.1	0.39
		Mn−Mn_1	4	2.89	9.6	
		Mn−Mn_2	4	3.4	11.2	
Co-γ-MnO_2	γ-MnO_2	Mn−O	5.7	1.89	3.0	1.99
		Mn−Mn_1	3.9	2.89	9.7	
		Mn−Mn_2	3.9	3.4	11.3	
Ce-γ-MnO_2	γ-MnO_2	Mn−O	5.3	1.89	3.0	2.01
		Mn−Mn_1	3.8	2.89	11.1	
		Mn−Mn_2	3.8	3.4	11.8	

[a]CN: coordination number. [b]R: bond distance [c]DW: Debye−Waller factor.

generated manganese and oxygen vacancies led to the appearance of coordinatively unsaturated [MnO_{6-x}] octahedra, which resulted in a distorted structure (Figure 4). The above results are consistent with the results revealed by HRTEM, H_2-TPR, O_2-TPD, XPS, and Raman.

According to the previous literature, an ozone decomposition mechanism based on the participation and recycling of oxygen vacancies is widely accepted.[16,57,58]

$$O_3 + V_O \rightarrow O_2 + O^{2-} \quad \text{(R2)}$$

$$O_3 + O^{2-} \rightarrow O_2 + O_2^{2-} \quad \text{(R3)}$$

$$O_2^{2-} \rightarrow O_2 + V_O \quad \text{(R4)}$$

Abundant surface oxygen vacancies on the surface of the catalyst could favor ozone decomposition. Hence, the presence of more surface oxygen vacancies was beneficial to the highly efficient removal of ozone on Ce-γ-MnO_2.

3.5. Ozone Decomposition Performance. Figure 9A shows the catalytic activity for ozone decomposition on γ-MnO_2 and M-γ-MnO_2 catalysts with relative humidity (RH) of 65%. Within 0.5 h, the activities of γ-MnO_2, Ce-γ-MnO_2, and Co-γ-MnO_2 were all above 90%, and there were no significant differences. However, the activity of α-MnO_2 and physically mixed α-MnO_2 and γ-MnO_2 (weight ratio 1:1) catalysts dropped sharply within 0.5 h. The α-MnO_2 catalyst showed

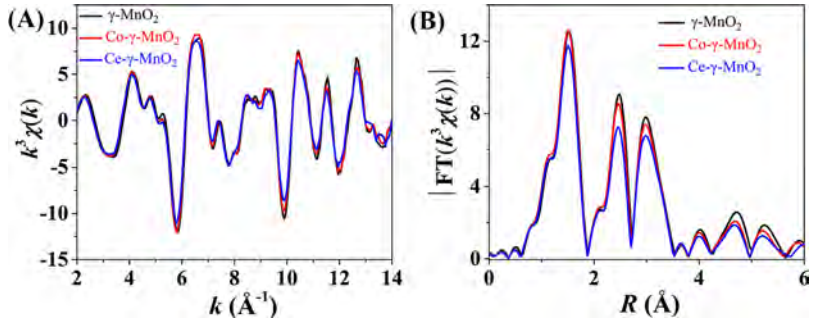

Figure 8. (A) Mn K-edge extended XAFS oscillation function $k^3\chi(k)$ and (B) the corresponding Fourier transforms FT($k^3\chi(k)$).

DOI: 10.1021/acs.est.8b04294
Environ. Sci. Technol. 2018, 52, 12685−12696

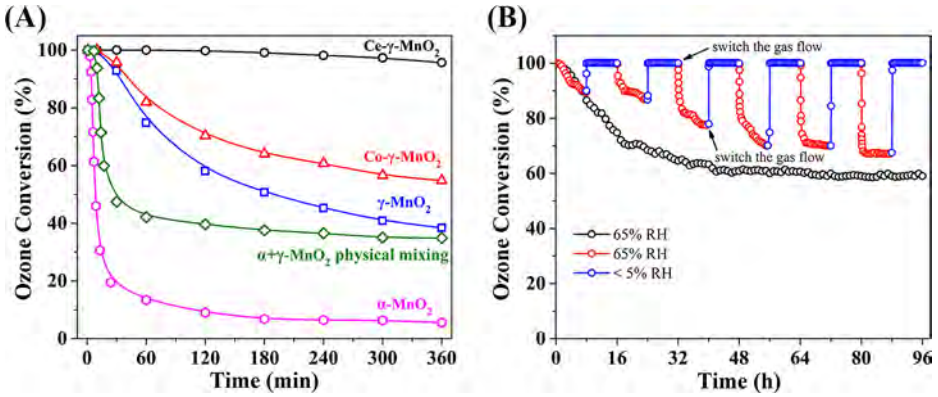

Figure 9. (A) The conversion of ozone on the γ-MnO_2, M-γ-MnO_2, α-MnO_2, and physically mixed α-MnO_2/γ-MnO_2 catalysts. Conditions: ozone inlet concentration 40 ppm, temperature 30 °C, RH = 65%, weight space velocity 840 L g^{-1} h^{-1}. (B) Durability of the Ce-γ-MnO_2 catalyst. Conditions: ozone inlet concentration 40 ppm, temperature 30 °C, weight space velocity 840 L g^{-1} h^{-1}.

less than 20% ozone conversion. After physical mixing of α-MnO_2 and γ-MnO_2, the catalytic activity only increased to about 45%. After 1 h, the ozone conversion of γ-MnO_2 and Co-γ-MnO_2 distinctly decreased, while the Ce-γ-MnO_2 catalyst still showed almost 100% ozone conversion. The activity of α-MnO_2 and physically mixed α-MnO_2/γ-MnO_2 catalysts was 14% and 43%, respectively. The Ce-γ-MnO_2 catalyst maintained 96% ozone conversion after 6 h. However, the ozone conversion on the Co-γ-MnO_2 and γ-MnO_2 catalysts was 55% and 38%, respectively. As shown in Figure S6, the activity of CeO_2 and Co_3O_4 was very poor, which indicates that the two components do not contribute to increasing the activity of the Ce-γ-MnO_2 or Co-γ-MnO_2 catalysts. The activity of α-MnO_2 was stable at 5% after 6 h, and the physically mixed α-MnO_2/γ-MnO_2 catalyst also had stable ozone conversion of about 35%, showing far less activity than Ce-γ-MnO_2. The above results indicate that Ce doping induced the formation of a mixed crystal during the synthetic process, which leads to superior activity compared to that obtained with the physically mixed catalyst. During the synthetic process of γ-MnO_2, the addition of transition metals destroyed the normal growth of crystals. The most logical source of the enhancement is the mixed crystal, amorphous regions and obvious local lattice distortions appearing in HRTEM images, which can increase the specific surface area and oxygen vacancies of the catalyst. However, simple physical mixing cannot change the crystal structure. According to the previous literature, oxygen vacancies play a key role in the catalytic decomposition of ozone. The above characterization indicates that the Ce-γ-MnO_2 catalyst has the most oxygen vacancies, so it has the best catalytic activity.

Considering its practical application in ozone decomposition, the Ce-γ-MnO_2 catalyst was continuously tested for longer time periods under RH = 65%. As shown in Figure 9 B, the removal efficiency of the Ce-γ-MnO_2 catalyst for 40 ppm ozone decreased slowly and ultimately maintained a level of 60% after a continuous 96 h test. However, the catalytic activity of the Ce-γ-MnO_2 catalyst always maintained a level of 100% under dry conditions, which indicates that the deactivation of the catalysts under RH = 65% conditions is mainly due to the competitive adsorption of water molecules and ozone molecules. The ozone removal rate evaluated under alternating humidity conditions is shown in Figure 9B. When the Ce-γ-MnO_2 catalyst was first placed in the wet gas flow (RH = 65%), the ozone conversion gradually decreased to 89% at the first cycle (8 h). However, when the gas path was switched to the dry atmosphere (RH < 5%), the ozone removal rate quickly recovered to 100%. Furthermore, when the RH was increased to 65% again, the ozone removal efficiency gradually reduced to the level of the first cycle (89%) in the first 6 h, and the ozone conversion slowly decreased to 86%, which indicates that water molecules are weakly adsorbed on the catalyst and can be blown away by the dry gas stream. When the Ce-γ-MnO_2 catalyst was placed in the wet gas flow a third time, the catalytic activity quickly dropped to the level of the second cycle in half an hour and then slowly decreased to 78% after 8 h. In the next few cycles, the catalytic activity quickly decreased to the level of the previous cycle, which could be because the oxygen vacancies able to decompose ozone were reduced. As is shown in Figure S7, the surface average oxidation state (AOS) of Mn of the ozone-treated Ce-γ-MnO_2 catalyst increased to 3.64, and the Mn^{3+} content of the ozone-treated Ce-γ-MnO_2 catalyst decreased to 14.68%, which indicates that the oxygen vacancies of the Ce-γ-MnO_2 catalyst decreased after ozone treatment.[16] This is because part of the oxygen species (from ozone molecules) adsorbed on the oxygen vacancies is not easily desorbed.[28] In order to test the stability of the catalyst under dry conditions, the decomposition of ozone on Ce-γ-MnO_2 was investigated under high space velocity. As is shown in Figure S8, the removal efficiency of the Ce-γ-MnO_2 catalyst ultimately maintained a level of 81% after a continuous 96 h test under the space velocity of 5600 L g^{-1} h^{-1} and dry gas. The above results further indicate that if the oxygen species (from ozone molecules) adsorbed on the oxygen vacancies cannot be desorbed in time, the catalyst will be gradually deactivated. As is shown in Figure 9B and Figure S8, the catalytic activity of the Ce-γ-MnO_2 catalyst eventually stabilized at a certain value, which indicates that a portion of the oxygen vacancies on the catalyst surface is stable and is not easily deactivated. Therefore, there are different types of oxygen vacancies on the catalyst surface, some of which are easily deactivated, and others are relatively stable. The oxygen vacancies weakly combined with intermediate oxygen species could be the more stable active sites. Even though the number of active sites was reduced, the catalyst still had 100% ozone conversion under dry conditions and weight space velocity of 840 L g^{-1} h^{-1}, which indicates that the remaining oxygen vacancies are very efficient active sites. Therefore, Ce-γ-MnO_2 has promising application potential in industry.

DOI: 10.1021/acs.est.8b04294
Environ. Sci. Technol. 2018, 52, 12685−12696

3.6. Implications and Future Direction of the Research. Transition metal (cerium and cobalt) doped γ-MnO_2 catalysts were successfully synthesized by reaction between the metal ions, Mn^{2+}, and $(NH_4)_2S_2O_8$ via a one-step hydrothermal method. Different metal-ion-doped M-γ-MnO_2 catalysts showed distinct differences in their ozone decomposition activities, which is mainly due to different contents of oxygen vacancies. The Ce-γ-MnO_2 materials were far superior to the Co-γ-MnO_2 and γ-MnO_2 catalysts, and the materials showed ozone (O_3) conversion of 96% for 40 ppm of O_3 under RH = 65% and space velocity of 840 L g^{-1} h^{-1} after 6 h at room temperature. A series of experimental results indicated that cerium-doped γ-MnO_2 can form more surface oxygen vacancies along with formation of a mixed crystal and an increase in the specific surface area, which further demonstrates the key role of oxygen vacancies in the catalytic decomposition of ozone.

In this work, the removal efficiency of the Ce-γ-MnO_2 catalyst for 40 ppm ozone under RH = 65% and space velocity of 840 L g^{-1} h^{-1} still remained at 60% ozone conversion after a continuous 96 h test, and the ozone conversion rate could reach 100% for 96 h under dry conditions and space velocity of 840 L g^{-1} h^{-1}, which indicates that the Ce-γ-MnO_2 catalyst possesses promising application potential in industry. Furthermore, the durability tests of the Ce-γ-MnO_2 catalyst show that the catalyst deactivation under a wet gas stream is mainly due to the competitive adsorption between water molecules and ozone molecules, and the catalyst deactivation under the dry gas stream is mainly due to the fact that part of the oxygen vacancies is easily deactivated. Therefore, if ozone molecules can be more easily adsorbed at the oxygen vacancies (weakening the competitive adsorption of water molecules), and the generated intermediate oxygen species are more easily desorbed (by synthesis of catalysts having oxygen vacancies weakly combined with intermediate oxygen species), the catalytic activity can be greatly enhanced, which provides guidance for the further improvement of catalysts.

■ ASSOCIATED CONTENT

Supporting Information

The Supporting Information is available free of charge on the ACS Publications website at DOI: 10.1021/acs.est.8b04294.

Characterization methods and other supplementary data (PDF)

■ AUTHOR INFORMATION

Corresponding Author

*E-mail: jzma@rcees.ac.cn.

ORCID

Jinzhu Ma: 0000-0003-1878-0669

Guangzhi He: 0000-0003-1770-3522

Changbin Zhang: 0000-0003-2124-0620

Notes

The authors declare no competing financial interest.

■ ACKNOWLEDGMENTS

This work was supported by the National Key R&D Program of China (2016YFC0207104, 2017YFC0211802), the National Natural Science Foundation of China (NSFC) (No. 21876191), and the Youth Innovation Promotion Association, CAS (2017064).

■ REFERENCES

(1) Gao, W.; Tie, X. X.; Xu, J. M.; Huang, R. J.; Mao, X. Q.; Zhou, G. Q.; Chang, L. Y. Long-term trend of O_3 in a mega City (Shanghai), China: Characteristics, causes, and interactions with precursors. *Sci. Total. Environ.* **2017**, *603−604* (4), 425−433.

(2) Phalitnonkiat, P.; Sun, W. X.; Grigoriu, M. D.; Hess, P.; Samorodnitsky, G. Extreme ozone events: Tail behavior of the surface ozone distribution over the US. *Atmos. Environ.* **2016**, *128*, 134−146.

(3) Lin, M. Y.; Horowitz, L. W.; Cooper, O. R.; Tarasick, D.; Conley, S.; Iraci, L. T.; Johnson, B.; Leblanc, T.; Petropavlovskikh, I.; Yates, E. L. Revisiting the evidence of increasing springtime ozone mixing ratios in the free troposphere over western North America. *Geophys. Res. Lett.* **2015**, *42* (20), 8719−8728.

(4) Fadeyi, M. O. Ozone in indoor environments: Research progress in the past 15 years. *Sustain. Cities. Soc.* **2015**, *18*, 78−94.

(5) Wang, H.; He, C. R.; Morawska, L.; McGarry, P.; Johnson, G. Ozone-initiated particle formation, particle aging, and precursors in a laser printer. *Environ. Sci. Technol.* **2012**, *46* (2), 704−712.

(6) Levy, J. I.; Carrothers, T. J.; Tuomisto, J. T.; Hammitt, J. K.; Evans, J. S. Assessing the public health benefits of reduced ozone concentrations. *Environ. Health. Perspect.* **2001**, *109* (12), 1215−1226.

(7) Kim, C. S.; Alexis, N. E.; Rappold, A. G.; Kehrl, H.; Hazucha, M. J.; Lay, J. C.; Schmitt, M. T.; Case, M.; Devlin, R. B.; Peden, D. B.; Diaz-Sanchez, D. Lung function and inflammatory responses in healthy young adults exposed to 0.06 ppm ozone for 6.6 h. *Am. J. Respir. Crit. Care Med.* **2011**, *183* (9), 1215−1221.

(8) Hoffmann, B.; Luttmann-Gibson, H.; Cohen, A.; Zanobetti, A.; de Souza, C.; Foley, C.; Suh, H. H.; Coull, B. A.; Schwartz, J.; Mittleman, M.; Stone, P.; Horton, E.; Gold, D. R. Opposing effects of particle pollution, ozone, and ambient temperature on arterial blood pressure. *Environ. Health Perspect.* **2012**, *120* (2), 241−246.

(9) LaCount, B. J.; Castro, J. M.; Ignatz-Hoover, F. Development of a service-simulating, accelerated aging test method for exterior tire rubber compounds II. Design and development of an accelerated outdoor aging simulator. *Polym. Degrad. Stab.* **2002**, *75* (2), 213−227.

(10) Naydenov, A.; Konova, P.; Nikolov, P.; Klingstedt, F.; Kumar, N.; Kovacheva, D.; Stefanov, P.; Stoyanova, R.; Mehandjiev, D. Decomposition of ozone on Ag/SiO_2 catalyst for abatement of waste gases emissions. *Catal. Today* **2008**, *137* (2−4), 471−474.

(11) Imamura, S.; Ikebata, M.; Ito, T.; Ogita, T. Decomposition of ozone on a silver catalyst. *Ind. Eng. Chem. Res.* **1991**, *30* (1), 217−221.

(12) Hao, Z. P.; Cheng, D. Y.; Guo, Y.; Liang, Y. H. Supported gold catalysts used for ozone decomposition and simultaneous elimination of ozone and carbon monoxide at ambient temperature. *Appl. Catal., B* **2001**, *33* (3), 217−222.

(13) Zhang, P. Y.; Zhang, B.; Shi, R. Catalytic decomposition of low level ozone with gold nanoparticles supported on activated carbon. *Front. Environ. Sci. Eng. China* **2009**, *3* (3), 281−288.

(14) Yu, Q.; Pan, H.; Zhao, M.; Liu, Z.; Wang, J.; Chen, Y.; Gong, M. Influence of calcination temperature on the performance of Pd-Mn/SiO_2-Al_2O_3 catalysts for ozone decomposition. *J. Hazard. Mater.* **2009**, *172* (2−3), 631−4.

(15) Kameya, T.; Urano, K. Catalytic decomposition of ozone gas by a Pd impregnated MnO_2 catalyst. *J. Environ. Eng-Asce.* **2002**, *128* (3), 286−292.

(16) Zhu, G. X.; Zhu, J. G.; Jiang, W. J.; Zhang, Z. J.; Wang, J.; Zhu, Y. F.; Zhang, Q. F. Surface oxygen vacancy induced alpha-MnO_2 nanofiber for highly efficient ozone elimination. *Appl. Catal., B* **2017**, *209*, 729−737.

(17) Tang, W. X.; Liu, H. D.; Wu, X. F.; Chen, Y. F. Higher oxidation state responsible for ozone decomposition at room temperature over manganese and cobalt oxides: Effect of calcination temperature. *Ozone: Sci. Eng.* **2014**, *36* (5), 502−512.

(18) Gong, S. Y.; Li, W. H.; Xie, Z.; Ma, X.; Liu, H. D.; Han, N.; Chen, Y. F. Low temperature decomposition of ozone by facilely

synthesized cuprous oxide catalyst. *New J. Chem.* **2017**, *41* (12), 4828−4834.
(19) Gong, S. Y.; Chen, J. Y.; Wu, X. F.; Han, N.; Chen, Y. F. In-situ synthesis of Cu_2O/reduced graphene oxide composite as effective catalyst for ozone decomposition. *Catal. Commun.* **2018**, *106*, 25−29.
(20) Mehandjiev, D.; Naidenov, A. Ozone decomposition on alpha-Fe_2O_3 catalyst. *Ozone: Sci. Eng.* **1992**, *14* (4), 277−282.
(21) Lian, Z. H.; Ma, J. Z.; He, H. Decomposition of high-level ozone under high humidity over Mn-Fe catalyst: The influence of iron precursors. *Catal. Commun.* **2015**, *59*, 156−160.
(22) Mehandjiev, D.; Naydenov, A.; Ivanov, G. Ozone decomposition, benzene and CO oxidation over $NiMnO_3$-ilmenite and $NiMn_2O_4$-spinel catalysts. *Appl. Catal., A* **2001**, *206* (1), 13−18.
(23) Dhandapani, B.; Oyama, S. T. Gas phase ozone decomposition catalysts. *Appl. Catal., B* **1997**, *11* (2), 129−166.
(24) Heisig, C.; Zhang, W. M.; Oyama, S. T. Decomposition of ozone using carbon-supported metal oxide catalysts. *Appl. Catal., B* **1997**, *14* (1−2), 117−129.
(25) Yang, Y.; Huang, J.; Wang, S. W.; Deng, S. B.; Wang, B.; Yu, G. Catalytic removal of gaseous unintentional POPs on manganese oxide octahedral molecular sieves. *Appl. Catal., B* **2013**, *142-143*, 568−578.
(26) Jia, J. B.; Zhang, P. Y.; Chen, L. The effect of morphology of alpha-MnO_2 on catalytic decomposition of gaseous ozone. *Catal. Sci. Technol.* **2016**, *6* (15), 5841−5847.
(27) Zhu, G. X.; Zhu, J. G.; Li, W. L.; Yao, W. Q.; Zong, R. L.; Zhu, Y. F.; Zhang, Q. F. Tuning the K+ concentration in the tunnels of alpha-MnO_2 to increase the content of oxygen vacancy for ozone elimination. *Environ. Sci. Technol.* **2018**, *52* (15), 8684−8692.
(28) Jia, J. B.; Zhang, P. Y.; Chen, L. Catalytic decomposition of gaseous ozone over manganese dioxides with different crystal structures. *Appl. Catal., B* **2016**, *189*, 210−218.
(29) Gong, P.; Xie, J.; Fang, D.; Han, D.; He, F.; Li, F.; Qi, K. Effects of surface physicochemical properties on NH_3-SCR activity of MnO_2 catalysts with different crystal structures. *Chinese. J. Catal.* **2017**, *38* (11), 1925−1934.
(30) Lin, H.; Chen, D.; Liu, H.; Zou, X.; Chen, T. Effect of MnO_2 crystalline structure on the catalytic oxidation of formaldehyde. *Aerosol Air Qual. Res.* **2017**, *17* (4), 1011−1020.
(31) Wang, T.; Chen, S.; Wang, H.; Liu, Z.; Wu, Z. In-plasma catalytic degradation of toluene over different MnO_2 polymorphs study of reaction mechanism. *Chinese. J. Catal.* **2017**, *38* (5), 793−804.
(32) Liu, Y. Y.; Chen, Z. W.; Shek, C. H.; Wu, C. M. L.; Lai, J. K. L. Hierarchical mesoporous MnO_2 superstructures synthesized by soft-interface method and their catalytic performances. *ACS Appl. Mater. Interfaces* **2014**, *6* (12), 9776−9784.
(33) Wang, C. X.; Ma, J. Z.; Liu, F. D.; He, H.; Zhang, R. D. The effects of Mn^{2+} precursors on the structure and ozone decomposition activity of cryptomelane-type manganese oxide (OMS-2) catalysts. *J. Phys. Chem. C* **2015**, *119* (40), 23119−23126.
(34) Gao, J. J.; Jia, C. M.; Zhang, L. P.; Wang, H. M.; Yang, Y. H.; Hung, S. F.; Hsu, Y. Y.; Liu, B. Tuning chemical bonding of MnO_2 through transition-metal doping for enhanced CO oxidation. *J. Catal.* **2016**, *341*, 82−90.
(35) Chen, C.; Xu, K.; Ji, X.; Zhang, B.; Miao, L.; Jiang, J. J. Enhanced electrochemical performance by facile oxygen vacancies from lower valence-state doping for ramsdellite-MnO_2. *J. Mater. Chem. A* **2015**, *3* (23), 12461−12467.
(36) Ma, J. Z.; Wang, C. X.; He, H. Transition metal doped cryptomelane-type manganese oxide catalysts for ozone decomposition. *Appl. Catal., B* **2017**, *201*, 503−510.
(37) Liu, Y.; Zhang, P. Y. Catalytic decomposition of gaseous ozone over todorokite-type manganese dioxides at room temperature: Effects of cerium modification. *Appl. Catal., A* **2017**, *530*, 102−110.
(38) Jia, J. B.; Yang, W. J.; Zhang, P. Y.; Zhang, J. Y. Facile synthesis of Fe-modified manganese oxide with high content of oxygen vacancies for efficient airborne ozone destruction. *Appl. Catal., A* **2017**, *546*, 79−86.
(39) Zhang, J.; Li, Y.; Wang, L.; Zhang, C.; He, H. Catalytic oxidation of formaldehyde over manganese oxides with different crystal structures. *Catal. Sci. Technol.* **2015**, *5* (4), 2305−2313.
(40) Xing, S. T.; Lu, X. Y.; Ren, L. M.; Ma, Z. C. Characterization and reactivity of Mn-Ce-O composites for catalytic ozonation of antipyrine. *RSC Adv.* **2015**, *5* (74), 60279−60285.
(41) Ide, Y.; Inami, N.; Hattori, H.; Saito, K.; Sohmiya, M.; Tsunoji, N.; Komaguchi, K.; Sano, T.; Bando, Y.; Golberg, D.; Sugahara, Y. Remarkable charge separation and photocatalytic efficiency enhancement through interconnection of TiO_2 nanoparticles by hydrothermal treatment. *Angew. Chem., Int. Ed.* **2016**, *55* (11), 3600−3605.
(42) Sun, M.; Yu, L.; Ye, F.; Diao, G. Q.; Yu, Q.; Hao, Z. F.; Zheng, Y. Y.; Yuan, L. X. Transition metal doped cryptomelane-type manganese oxide for low-temperature catalytic combustion of dimethyl ether. *Chem. Eng. J.* **2013**, *220*, 320−327.
(43) Wang, S. M. Effects of Fe on crystallization and properties of a new high infrared radiance glass-ceramics. *Environ. Sci. Technol.* **2010**, *44* (12), 4816−4820.
(44) Liu, S. L.; Ji, J.; Yu, Y.; Huang, H. B. Facile synthesis of amorphous mesoporous manganese oxides for efficient catalytic decomposition of ozone. *Catal. Sci. Technol.* **2018**, *8* (16), 4264−4273.
(45) Wang, Q.; Chen, L. F.; Guan, S. L.; Zhang, X.; Wang, B.; Cao, X. Z.; Yu, Z.; He, Y. F.; Evans, D. G.; Feng, J. T.; Li, D. Q. Ultrathin and vacancy-rich coal-layered double hydroxide/graphite oxide catalysts: Promotional effect of cobalt vacancies and oxygen vacancies in alcohol oxidation. *ACS Catal.* **2018**, *8* (4), 3104−3115.
(46) Yang, Y.; Zhang, S. Z.; Wang, S. W.; Zhang, K. L.; Wang, H. Z.; Huang, J.; Deng, S. B.; Wang, B.; Wang, Y. J.; Yu, G. Ball milling synthesized MnO_x as highly active catalyst for gaseous POPs removal: Significance of mechanochemically induced oxygen vacancies. *Environ. Sci. Technol.* **2015**, *49* (7), 4473−4480.
(47) Wang, F.; Dai, H. X.; Deng, J. G.; Bai, G. M.; Ji, K. M.; Liu, Y. X. Manganese oxides with rod-, wire-, tube-, and flower-like morphologies: Highly effective catalysts for the removal of toluene. *Environ. Sci. Technol.* **2012**, *46* (7), 4034−4041.
(48) Ma, Z. C.; Wei, X. Y.; Xing, S. T.; Li, J. S. Hydrothermal synthesis and characterization of surface-modified delta-MnO_2 with high Fenton-like catalytic activity. *Catal. Commun.* **2015**, *67*, 68−71.
(49) Chen, H.; Wang, Y.; Lv, Y. K. Catalytic oxidation of NO over MnO_2 with different crystal structures. *RSC Adv.* **2016**, *6* (59), 54032−54040.
(50) Xie, Y.; Yu, Y.; Gong, X.; Guo, Y.; Guo, Y.; Wang, Y.; Lu, G. Effect of the crystal plane figure on the catalytic performance of MnO_2 for the total oxidation of propane. *CrystEngComm* **2015**, *17* (15), 3005−3014.
(51) Gao, T.; Fjellvag, H.; Norby, P. Structural and morphological evolution of beta-MnO_2 nanorods during hydrothermal synthesis. *Nanotechnology* **2009**, *20* (5), 055610.
(52) Wang, R. H.; Li, J. H. OMS-2 catalysts for formaldehyde oxidation: Effects of Ce and Pt on structure and performance of the catalysts. *Catal. Lett.* **2009**, *131* (3−4), 500−505.
(53) Xu, J.; Li, P.; Song, X. F.; He, C. H.; Yu, J. G.; Han, Y. F. Operando raman spectroscopy for determining the active phase in one-dimensional $Mn_{1-x}Ce_xO_{2+y}$ nanorod catalysts during methane combustion. *J. Phys. Chem. Lett.* **2010**, *1* (10), 1648−1654.
(54) Julien, C.; Massot, M.; Rangan, S.; Lemal, M.; Guyomard, D. Study of structural defects in gamma-MnO_2 by Raman spectroscopy. *J. Raman Spectrosc.* **2002**, *33* (4), 223−228.
(55) Gao, S.; Sun, Z. T.; Liu, W.; Jiao, X. C.; Zu, X. L.; Hu, Q. T.; Sun, Y. F.; Yao, T.; Zhang, W. H.; Wei, S. Q.; Xie, Y. Atomic layer confined vacancies for atomic-level insights into carbon dioxide electroreduction. *Nat. Commun.* **2017**, *8*, 14503.
(56) Wang, J.; Lin, L. X.; He, Y.; Qin, H. Y.; Yan, S.; Yang, K.; Li, A. G.; Liu, J. B. Vacancy-assisted oxygen reduction reaction on cobalt-based catalysts in direct borohydride fuel cell revealed by in-situ XAFS and XRD. *Electrochim. Acta* **2017**, *254*, 72−78.
(57) Ding, Y. H.; Zhang, X. L.; Chen, L.; Wang, X. R.; Zhang, N.; Liu, Y. F.; Fang, Y. Z. Oxygen vacancies enabled enhancement of

DOI: 10.1021/acs.est.8b04294
Environ. Sci. Technol. 2018, 52, 12685−12696

catalytic property of Al reduced anatase TiO_2 in the decomposition of high concentration ozone. *J. Solid State Chem.* **2017**, *250*, 121−127.
(58) Li, W.; Gibbs, G. V.; Oyama, S. T. Mechanism of ozone decomposition on a manganese oxide catalyst. I. In situ Raman spectroscopy and ab initio molecular orbital calculations. *J. Am. Chem. Soc.* **1998**, *120* (35), 9041−9046.

DOI: 10.1021/acs.est.8b04294
Environ. Sci. Technol. 2018, 52, 12685−12696